Semiconductor Detector

Santiago R., Birge Sükrü Tok, Mattis Roost [1]
[1] *Physics Institute, Humboldt University Berlin, Germany*
Instructor: Dr. Marzieh Bahmani
(Hand-In Date: June 30, 2021; Experiment Date: 3.6.2021)

Semiconductor detectors are devices that use a semiconductor materials like silicon or germanium to measure ionizing radiation by means of the photoelectric effect. Such a high purity germanium Mirion GC2018 detector was used in this experiment to measure the characteristic spectra of ^{60}Co, ^{137}Cs, ^{133}Ba and ^{241}Am isotope samples, with the source activity of the ^{137}Cs sample also being computed as $A_{Cs-137} = (230 \pm 6)$ kBq. Furthermore, a characterization of the detector itself was carried out. Those measurements led to an estimated relative efficiency $\epsilon_{rel} = 18\%$ and an energy resolution (FWHM) of 2.83 for a 1.3 MeV energy peak. The energy dependence of this FWHM and the detectors peak-to-Compton ratio was measured as well. Lastly, the mass attenuation coefficients μ of aluminium μ_{Al}, copper μ_{Co}, molybdenum μ_{Mo} and lead μ_{Le} were inferred from changes in the measured intensities when placing different thicknesses of those materials between the ^{133}Ba isotope and the detector.

I Introduction

I.1 Theory

Gamma radiation is comprised of high energy photons emitted by atomic nuclei during decay and fusion processes. It is one of the three types of radiation observed around radioactive isotopes, alongside the $\alpha-$ and β radiation comprised of ^4_2He nuclei and electrons/positrons respectively instead of photons. For this experiment, the following interactions of gamma radiation with matter were of relevance.

I.1.1 Photoelectric Effect

High energy photons are capable of ionizing atoms N in a given material. An electron e^- that is bound to an atom can absorb the energy of a photon and leave the atom, if the photon energy exceeds the binding energy between the atom and the electron. If an electron is emitted due to this photoelectric effect the difference in energy between the absorbed photon energy and the binding energy is stored in the kinetic energy of the then free electron.

$$\gamma + N \rightarrow N^+ + e^- \tag{1}$$

This effect is dominant at lower γ-energies ($E_{Ph} < 0.1MeV$) where the rate of interaction between the photons and bound electrons is at its highest. This inverse proportionality can be seen as well in the cross section for this interaction which is given by [1]

$$\sigma = a \cdot \frac{Z^n}{E_\gamma^m} \tag{2}$$

where a is a constant and $m = \frac{7}{2}$, $n = 4...5$ for $E_\gamma \in [0.1, 5]MeV$. At higher energies, the photoelectric effect competes with Compton scattering and pair-production processes, so the cross section must be computed differently.

I.1.2 Compton Scattering

Compton scattering can occur whenever a photon interacts with a free charged particle - i.e. an unbound electron. It then only transfers part of its total energy E_γ to the charged particle, resulting in a decrease of its energy instead of a complete absorption as well as a change in the direction of propagation. The reaction is thus

$$\gamma + e^- \rightarrow \gamma' + e^{-\prime} \tag{3}$$

The amount of transferred energy depends on the scattering angle θ and the photon energy E_γ. The photon energy E'_γ after the interaction is then given by

$$E'_\gamma(\theta) = \frac{E_\gamma}{1 + (E_\gamma/m_e c^2)(1 - \cos\theta)} \tag{4}$$

The transfer of energy to the electron is thus at a maximum for $cos(\theta) = -1 \Rightarrow \theta = 180°$. Therefore, there is also a maximum of energy that can be detected due to a single Compton scattering. This so called Compton energy can be computed from the following formula:

$$E_{Compton} = E_\gamma \left(1 - \frac{1}{1 + 2E_\gamma/m_e c^2}\right) \tag{5}$$

All the Compton scattered photons contribute to a fairly continuous signal background (Compton continuum) which ends at the Compton energy. This gives rise to a more or less sharp drop off in the observed spectrum which is also called the Compton edge.

I.1.3 Pair Production

Lastly, pair production is the dominant form of photon interaction with matter at high γ-energies. It allows for positron-electron pairs to be generated during interactions between the photons and nuclei in the material such that;

$$N + \gamma \rightarrow N + e^- + e^+ \tag{6}$$

Due to conservation of energy, this is only possible for photons with energies greater than $2m_e c^2$.

$$E_\gamma = E_{kin} + 2m_e c^2 \tag{7}$$

where E_{kin} is the leftover energy now carried as kinetic energy by the produced pair and the recoiling nuclei.

I.2 Setup

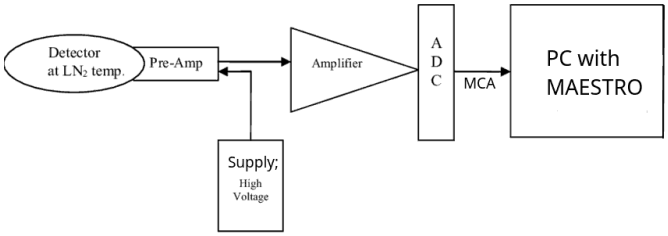

Figure 1: Setup Diagram

For this experiment, a high purity germanium detector (HPGe) - a MIRION GC2018 model - was used to measure the Gamma spectrum of a set of materials. The detector is connected to a high voltage supply and has its output amplified prior to being converted by an Analog-Digital converter (ADC) to be analyzed by a Multi-Channel Analyzer (MCA). It is lastly fed to a computer with the MAESTRO spectra analyzer software for displaying and data storage.

A p-type high purity germanium detector like the one used in this experiment utilizes the properties of a germanium semiconductor diode in reverse bias voltage to detect ionizing radiation. This diode is comprised of a germanium crystal that is divided into a p-type and a n-type region. At the pn-junction between the lightly doped p-type germanium crystal that constitutes the main part of the diode and the very thin layer of highly doped n-type germanium a depleted region arises. In this region the charge carriers of the p-type and the n-type materials have recombined creating an area without free charge carriers which therefore acts like an insulator.

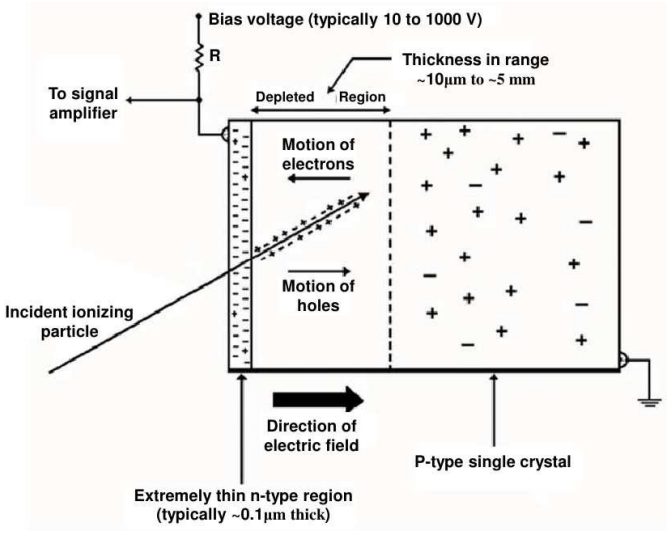

Figure 2: Schematic of a P-Type Semiconductor Detector

The depleted region constitutes the sensitive volume of the detector. When ionizing radiation interacts with material of the sensitive volume, it creates electron-hole pairs. That means that electrons in the valence band of the crystal absorb energy to move up into the almost completely empty conduction band leaving behind a holes in the valence band. Those holes then behave like positively charged electrons. As a result of the revers bias voltage the holes and the electrons move in opposite directions creating a small electrical current that can then be measured. The small band gaps of semiconductor materials allow for relatively high energy resolutions but make it also necessary to cool down the detector to very low temperatures to prevent thermal excitations of electrons into the conduction band which would lead to noise in the signal. In this case liquid nitrogen was used to cool down the detector to around 77 K.

The different samples ware placed in front of the detector. The distances were chosen such that the relative dead time of the detector did not exceed 3%. Depending on the measurement different absorbing materials were put in between. The radiation sources used and their previously measured values from ca. 1996 as given in [1] are listed below;

Nuclide	Activity in kBq	Uncertainties in %	Half-life
Am-241	375	4	432.2 y
Ba- 133	397	5	3854.7d
Cs-137	371	4	11018.3d
C0-60	470	4	1925.20d

Figure 3: List of radiation sources and parameters [1]

II Spectra of Gamma Isotopes

II.1 Energy to Channel Calibration

The first step in the analysis of the measured data was to obtain the count rates from the total count numbers. For this purpose, the total count numbers of each channel were divided by the respective measurement times (Live-Time) stored alongside the count data in each MAESTRO .std file. Since radioactive decay follows a Poisson distribution, the statistical uncertainties were computed from the total count number N and the measurement time t utilizing the following formula:

$$\Delta r = \frac{\sqrt{N}}{t} \tag{8}$$

Furthermore, the count rates of the background spectrum were subtracted from the spectra of the different isotopes in order to obtain reduced spectra with the least possible background noise. Since the statistical uncertainties of the count rates themselves follow a Gaussian distribution, the uncertainties of the count rates of the isotopes reduced by the count rates of the background were inferred using the standard error propagation formula.

To calibrate the MCA scale in units of keV, the full energy peaks of the four sources were fitted with Gaussian functions to extract the channel numbers of the peak locations and their respective standard deviations. Those values were fitted to the literature values of the γ-energies[4] of the respective sources.

Table 1: Positions of full energy peaks and their γ-energies

Channel number	γ-energy in keV
172.8 ± 1.3	59.5409 ± 0.0001
236.0 ± 1.3	80.9979 ± 0.0011
812.7 ± 1.4	276.3989 ± 0.0012
890.6 ± 1.4	302.8508 ± 0.0005
1046.7 ± 1.6	356.0129 ± 0.0017
1128.7 ± 1.6	383.8485 ± 0.0012
1948.1 ± 2.0	661.657 ± 0.003
3455.2 ± 2.6	1173.228 ± 0.003
3924.8 ± 2.6	1332.492 ± 0.004

$\Rightarrow$ slope of fit : m = (0.339308 ± 0.00024) keV/Chn
$\Rightarrow$ y-intercept of fit : b = (0.78 ± 0.07) keV

II.2 Compton Edge of Cs-137

From those fit parameters and the channel number (c) of the full energy peak of the Cs-137 peak the γ-energy of the Cs-137 source was calculated to be:

$$E_{\gamma,Cs-137} = (661.77 \pm 0.09)\ \text{keV}$$

However, one may notice various other peaks besides the main one in the recorded gamma spectrum. As explained previously in section I., when a photon scatters off of the detector material due to the Compton effect and escapes the detector afterwards, only a fraction of the photon energy is registered during the measurement. The amount of energy E' transferred is given by equation (4) and depends on the scattering angle $\theta \in [0°, 180°]$ resulting an Compton continuum seen as a plateau within the spectrum. The Compton energy of ^{137}Caesium was calculated with formula (5) and is marked by the orange line in Fig 4.

$$E_{Compton,Cs-137} = (477.44 \pm 0.5)\ \text{keV}$$

II.3 Source Activity of Cs-137

To estimate the activity of the source, the count rate of the energy spectrum of Cs-137 was integrated to compute the total counts R registered from the source. The parts of the spectrum with a low signal-to-noise ratio and above of the main peaks energy range were excluded however, since only the counts from the Cs-137 sample mattered. The total count rate R was given by

$$R = (1006.4 \pm 1.4)\frac{1}{s}$$

The solid angle Ω covered by the detector was calculated using the distance between the middle of the detector and the source (distance between end cap of the detector and sample d + depth of detector h), along with the detector diameter D indicated in the datasheet;

$$\Omega = arctan\left(\frac{D}{2(d+h)}\right) \tag{9}$$

The fraction of photons travelling within that solid angle was given by $\frac{\Omega}{4\pi}$. The activity could then be calculated with the following equation:

$$A(R,\Omega) = \frac{R}{sin(\Omega/2)^2} \tag{10}$$

During the experiment, the distance between the source and the detector end cap was (15.3 ± 0.2) cm. In the detector detasheet a depth of 4.9 cm and a diameter of 4.73 cm were specified. With this data and the integrated count rate R_{total} the activity of the Cs-137 source was calculated to be

$$A_{Cs-137} = (230 \pm 6)\text{kBq}$$

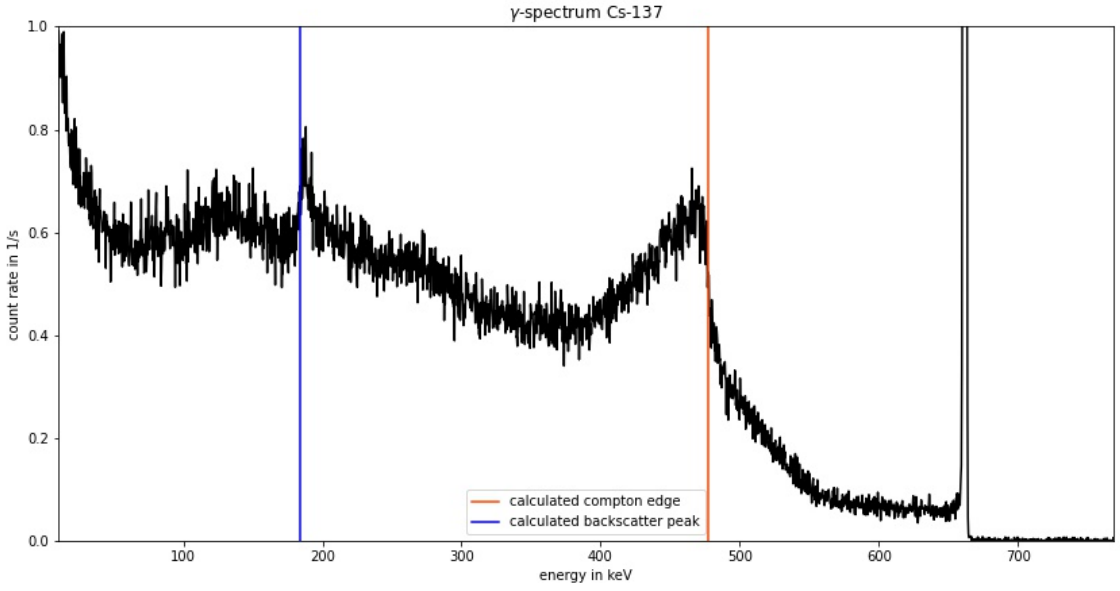

Figure 4: reduced γ-spectrum of Cs-137

II.3.1 Irradiation Dose

The irradiation dose each person received during the experiment was also estimated from this value assuming a body, consisting entirely of water, being irradiated 3 meters away from the Cs-137 source for 8 hours. From figure 1 in reference [1], the total mass absorption coefficient μ_a and the Compton scatter coefficient μ_{cs} for γ-energies around 660 keV in water were extracted as:

$$\mu_a = 0.0032 \frac{\text{cm}^2}{\text{g}} \quad \mu_{cs} = 0.004 \frac{\text{cm}^2}{\text{g}}$$

The total mass attenuation coefficient was therefore given by $\mu = \mu_a + \mu_{cs}$. The radiation intensity I obeys the following equation:

$$I(x) = I_0 \exp\left[-\mu \cdot \rho \cdot x\right] \tag{11}$$

In this expression, I_0 is the initial intensity of the radiation, ρ is the density of the material and x is the distance travelled by the photons. Since the intensity is proportional to the number of photons, the interaction rate in the body can be calculated using the following formula:

$$R_i = A_{Cs-137} \cdot f \cdot (1 - \exp\left[-\mu \cdot \rho_{water} \cdot x_{body}\right]) \tag{12}$$

In this expression, f is the fraction of solid angle covered by the body, x_{body} its depth and ρ_{water} is the density of water given by $0.997 \frac{\text{g}}{\text{cm}^3}$ [5].

For the photons that undergo Compton scattering, it was assumed that half of the Compton energy is deposited within the body on average. The fraction of photons that undergo Compton scattering is given by $\frac{\mu_{cs}}{\mu}$, whereas the fraction of photons that get absorbed is $\frac{\mu_a}{\mu}$. Consequently, the estimated energy absorbed by the body (with approximated dimensions: height=150cm, width=45cm, depth=30cm) after 8 hours of irradiation was:

$$\begin{aligned} E_{absorbed} &= 8 \cdot 3600 \text{ s} \cdot R_i \cdot \left(\frac{\mu_a}{\mu} E_{\gamma,Cs-137} \right. \\ &\quad \left. + \frac{\mu_{cs}}{\mu} 0.5 \cdot E_{Compton,Cs137} \right) \\ &= 8 \cdot 3600 \text{ s} \cdot 257.3 \text{ s}^{-1} \cdot \left(\frac{3.2}{7.2} \cdot 661.77 \text{ keV} \right. \\ &\quad \left. + \frac{4}{7.2} \cdot 238.72 \text{ keV} \right) \\ &\approx 3.2 \cdot 10^9 \text{ keV} \approx 5.1 \cdot 10^{-7} \text{ J} \end{aligned}$$

This results in an absorbed dose (quality factor times absorbed energy per mass) of approximately $2.5 \cdot 10^{-7}$ rad.

III Background Spectrum

The spectrum of background radiation sources was measured for more than one hour on the same day of the experiment. Figure 5 shows the count rates of the different γ-rays, that were detected.

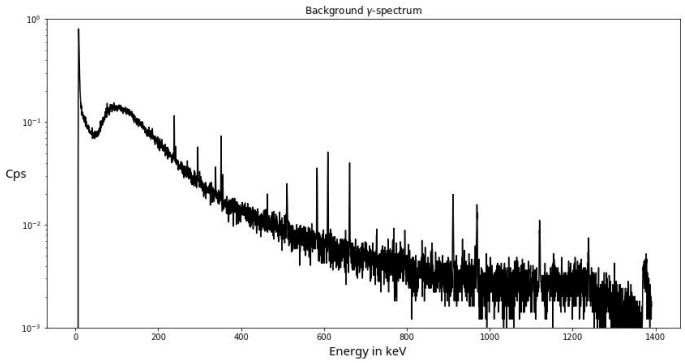

Figure 5: background γ-spectrum (Live-time: 4949 s)

The several sharp peaks, that are visible in the spectrum, come from the following sources:

Table 2: Sources of background radiation and their γ-energies[5]

Source	γ-energy (keV)	Source	γ-energy (keV)
^{212}Pb	238.36	^{214}Bi	609.31
^{224}Ra	240.99	^{137}Cs	661.77
^{214}Pb	242.0	^{212}Bi	727.33
^{212}Pb	295.22	^{228}Ac	794.59
^{228}Ac	338.32	^{228}Ac	911.2
^{212}Pb	351.93	^{214}Bi	934.06
^{228}Ac	363.0	^{228}Ac	968.97
^{208}Tl	510.77	^{214}Bi	1120.29
^{208}Tl	583.19	^{214}Bi	1238.11

IV Characterization of the Germanium Detector

For the characterization of the high purity germanium detector in this experiment, a variety of measures can be considered of relevance. For one, the IEEE standards relative detector efficiency, where the absolute efficiency of the detector as given below is compared to the efficiency of a Sodium Iodide (NaI) detector.

Another measure lies in the shape and quality of the data outputted by the detector; from this, one can infer the detectors energy resolution, given by the "Full Width at Half Maximum" (FWHM) of the ideally delta-like data peaks, and the Peak-to-Compton Ratio, which gives the relationship between the signal strength of the detected energy peaks and the detected lower energy photons from inelastic collisions in the Compton effect.

IV.1 Relative Detector Efficiency

The relative efficiency is computed by taking the number of particles recorded and dividing them by the number of quanta emitted by the source - in this case Cobalt-60 (^{60}Co) at a distance of 25cm to the detector end cap.

As the amount of quanta emitted is dependent on the activity of the source, this activity value is needed. This can be measured too or if previously measured already, the relevant value extracted from the given data. For the sample used, it was possible to do the latter. However, since a considerable amount of time

upwards of a decade has passed since the standardization of the samples, the activity will have dropped in a non-negligible amount due to the loss of material caused by radiation. By using the proportionality between material amount and activity, this loss may be accounted for using the following formula from the exponential decay equation:

$$A = A_0 e^{-\lambda t} = A_0 2^{-t/t_{1/2}} \tag{13}$$

where A_0 represents the measured activity in 1996 as given in figure 3, t the time elapsed since that measurement and $t_{1/2}$ the half life of ^{60}Co.

For this measurement, the 1.3 MeV emission of ^{60}Co is observed, through data taken for about 10 minutes. As this emission has a known probability of $P(\gamma_{1.3})$, this needs to be included during the emission calculation as well.

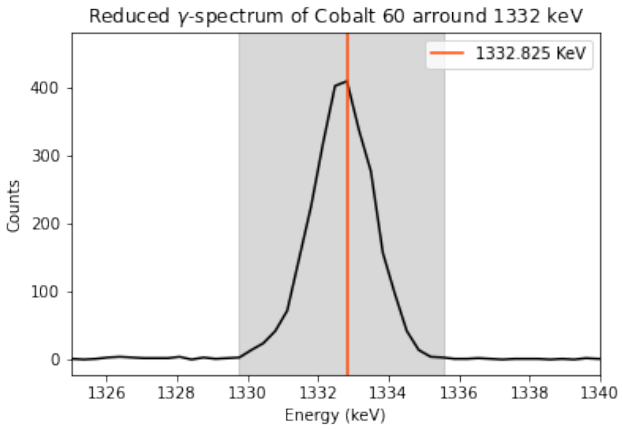

Figure 6: ^{60}Co γ-spectrum measurement (Live-time: 607 s)

Finally, this value is divided by the efficiency of a NaI detector ($1.2\ 10^{-3}$), yielding the following final equation for the relative efficiency:

$$\epsilon_{rel} = \frac{N}{TA\ 2^{-t/t_{1/2}} P(\gamma_{1.3})} \tag{14}$$

This results in a relative detector efficiency of around 18% for the Mirion GC2018 detector used here, which is close to the efficiency of 20% claimed by the manufacturer. However, the efficiency given by the "rule of thumb" $17\text{cm}^{-3} \cdot d$ returns an efficiency of 32 % when using the detector diameter given by the laboratory instructions, 75% when using the end cap diameter given by the datasheet of the GC2018, and 17% when using the diameter given in the SILENA datasheet. To be able to use this rule of thumb, the actual detector diameter of this detector is needed, however, it seems the diameter given varies strongly from document to document.

IV.2 Energy Resolution (FWHM)

After the relative detector efficiency, the energy resolution is also of major importance for the characterization of a semiconductor detector. It determines how close two emission energy peaks can be while still being separately measurable with a good certainty.

For the Cobalt peak, a FWHM of 2.83 is measured from the data-set below.

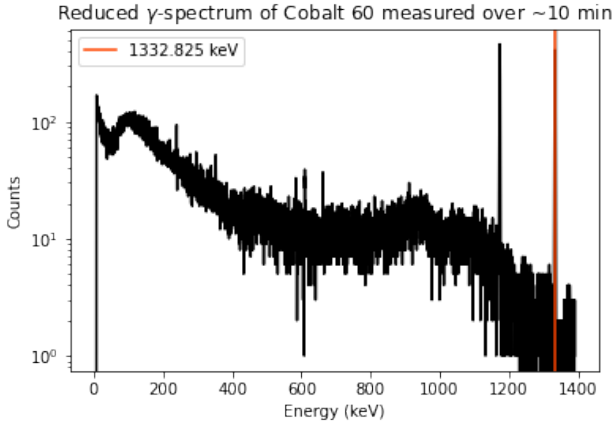

Figure 7: ^{60}Co γ-peak at 1.3MeV (Live-time: 607 s)

This energy resolution has 3 contributors, one of which is strongly dependent on the γ-ray energy.

$$\sigma^2_{FWHM} = \sigma^2_{E_\gamma} + \sigma^2_{collisions} + \sigma^2_{noise} \tag{15}$$

The other two are made out of random collision events and electric noise respectively.

To investigate the effect of this energy dependence, the FWHM is plotted at different energies. Here, the energy independent contributors were assumed as constant, and the energy proportional to the FWHM. Thus the following fit model $y = (ax)^2 + b$ was used to plot the dependence as shown below

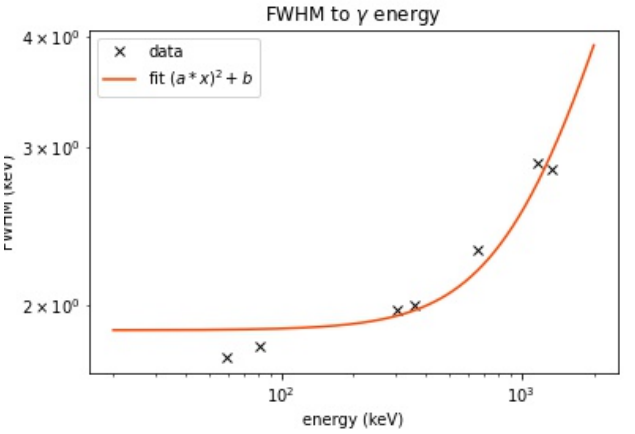

Figure 8: FWHM to Energy plot with 59.5, 80.9, 303.1, 3h6, 661, 1173, 1332.8 keV emissions

From this it becomes apparent that the resolution is not constant and increases in an exponential-like manner as the energy increases, meaning that at higher energies the expected resolution of the detector is lower.

IV.3 Peak-to-Compton Ratio

Finally, the peak-to-Compton ratio is examined and its energy dependence discussed as well. Unfortunately, for the measured $^{1}33Ba$ and $^{2}41Am$ spectra the Compton plateau was not apparent. For the former, the

Compton plateaus are interlocking, making a determination difficult, and with the later the noise peak at lower energies drowns out its Compton plateau. Thus the following analysis consists of only 3 different energies.

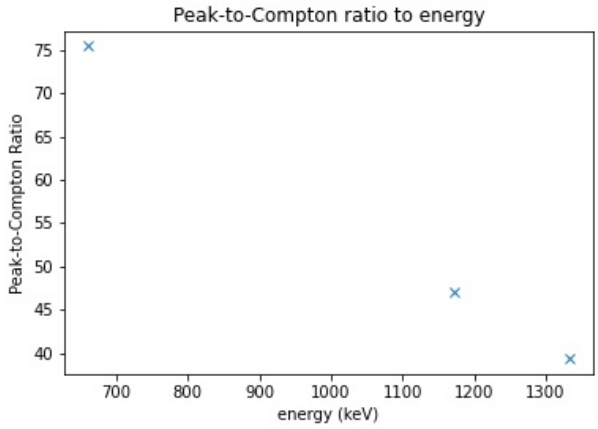

Figure 9: Measurements of Peak-to-Compton ratio w.r.t. energy at 661, 1173, 1332 keV

This data suggests a decreasing tendency of the peak-to-Compton ratio as the energy increases. A comment on linearity despite an apparent trend seems premature however, as there are too few data points for an accurate assessment.

A critical point may exist at the pair production threshold, as after that point some photons are lost to pair production instead, leading to a dip in the Compton continuum and thus a lower Peak-to-Compton ratio. Depending on the relative energy loss, this may not even be noticeable.

V Mass Attenuation

V.1 Mass Attenuation Coefficient μ of different Materials

Incoming radiation can be attenuated by shielding through different materials of varying thickness. The shielding from radiation provided by these materials depends on both the energy E_γ of the incoming radiation as well as the material properties such as density ρ, atomic number Z_n, mass attenuation coefficient μ and thickness d. For these parameters, the relation between these is given by

$$\frac{I}{I_0} = exp[-(\mu/\rho)\rho d] \tag{16}$$

where $\frac{I}{I_0}$ gives the fraction of the measured radiation intensity I after being attenuated to the original intensity of the outgoing radiation from the probe I_0. The energy and atomic number dependence is implied by $\mu = \mu(E_\gamma, Z_n)$. These two intensities were measured for the following materials sheets of thickness d $[mm \pm 0.1]$ at distance D using the ^{133}Ba sample as a radioactive source.

Source	D	d_1	d_2	d_3	d_4	d_5
Aluminium	10.3 cm	0.5	0.85	2	4	6
Copper	10.3 cm	0.5	1	3	4.5	
Lead	8.2 cm	1	1.5	2	3	4
Molybdenum	9.1 cm	0.4	1.1	1.9	3.4	

Table 3: List of attenuation materials

Eq.(14) can be linearized by computing the natural logarithm of the measured intensities as shown below

$$ln(I_0/I) = \mu d + b \tag{17}$$

Such that the linearly fitted parameter for the slope gives the mass attenuation coefficient μ. One such example can be found below for aluminium at the main energies of $81keV$ and $356.02keV$ of the ^{133}Ba spectrum. The measured signal ratio was computed from the integral of the Gaussian-like peaks detected by an algorithm at the relevant energy channels in the background reduced data.

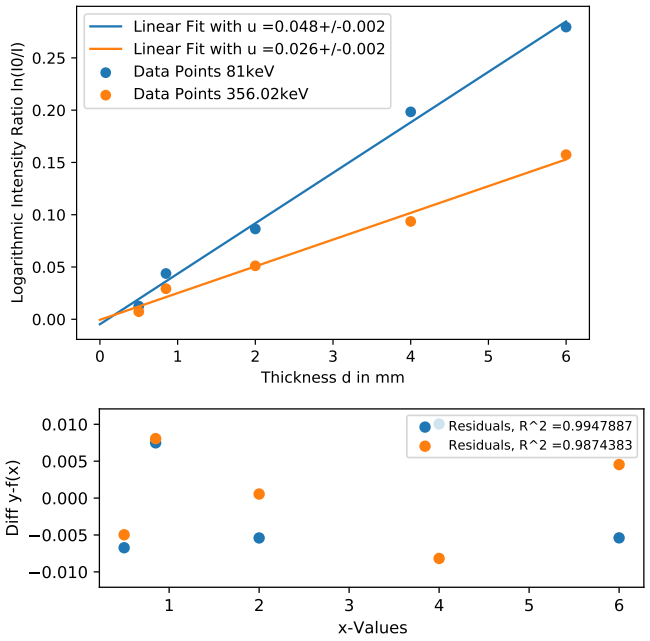

Figure 10: Aluminium Intensity Ratios $ln(I_0/I) = \mu(E_\gamma)d + b$

As expected, these data points followed a linear trend and were fitted accordingly. An exception to this was the plot and fitting attempt for the measurements using lead as the attenuating material, which resulted in a strongly non-linear shape of the data points and thus an inadequately shaped fit.

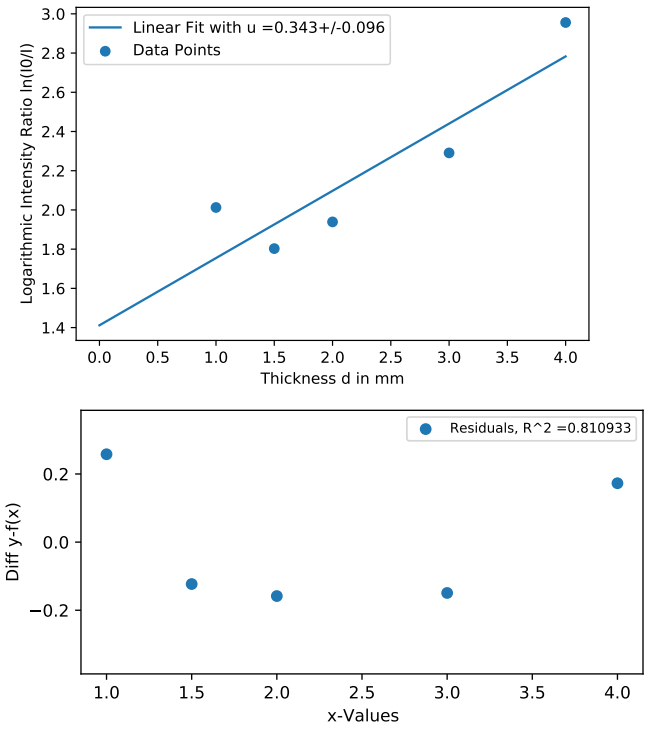

Figure 11: Lead Intensity Ratios $ln(I_0/I) = \mu(E_\gamma)d + b$

Furthermore, only data on the ratio of the radiation intensity for the energy peak at 81 keV could be computed, as any peaks at 356.02 keV that the algorithm could recognize were drowned out within the remaining background even after the background noise reduction. These unexpected results and their possible causes shall be emphasized further during the discussion.

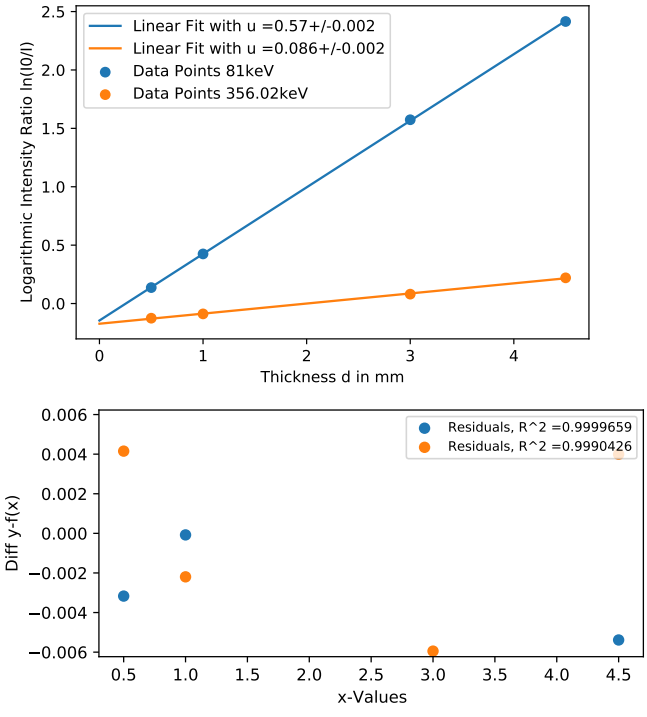

Figure 12: Copper Intensity Ratios $ln(I_0/I) = \mu(E_\gamma)d + b$

Repeating the same procedure for the data-sets recorded for copper above and molybdenum below yielded the following plots and fits.

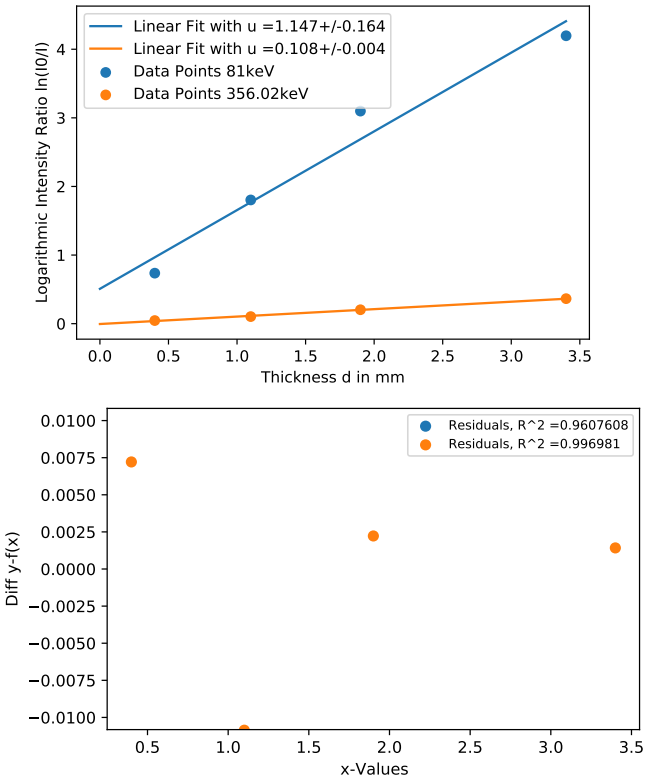

Figure 13: Molybdenum Intensity Ratios $ln(I_0/I) = \mu(E_\gamma)d + b$

As with aluminum and in contrast again to lead, both of these show a visually linear relationship between the logarithmic intensity ratios and material thicknesses. From the linear fits above, the following mass attenuation coefficients were computed for the materials used. The uncertainties were estimated through fitting algorithms inbuilt functions for error estimation in the fit parameters for each data-set.

Source	81 keV	356.02 keV
Aluminium	0.048 ± 0.002	0.0255 ± 0.0016
Copper	0.57 ± 0.0024	0.0864 ± 0.0019
Lead	(0.3 ± 0.1)?	no signal
Molybdenum	1.1 ± 0.2	0.108 ± 0.004

Table 4: Measured attenuation coefficients μ in 1/mm

V.2 Dependence on the Cross Section σ

For small energies around and below $0.1MeV$ where the photoelectric effect dominates the of photon-matter interactions, the relationship given in equation (2) for the cross section is valid up to small deviations σ_{noise} when describing the total cross section measured during the experiment such that

$$\sigma = a\frac{Z^n}{E_\gamma^m} + \sigma_{noise} \ , \ m = 7/2, n = 4...5 \qquad (18)$$

This produces a linear relationship between the cross section and the fraction $\frac{Z^n}{E_\gamma^m}$ of the atomic number Z of

the material used and the photon energy E_γ. Furthermore, one expects the following relation between the previously measured attenuation coefficients and the cross section [1]

$$\sigma = \mu \cdot \frac{A}{\rho \cdot N_A} \tag{19}$$

where ρ is the density of the material and A the molar mass along with the Avogadro constant N_A. From those formulas and through a linear fitting procedure, the following values for the proportionality factor a were computed using the measured attenuation coefficients in section V.2;

Source	σ (81 keV)	σ (356.02 keV)	a
Al	$(8.01 \pm 0.03)b$	$(4.24 \pm 0.02)b$	$-634.32 \frac{b}{keV}$
Co	$(67.1 \pm 0.05)b$	$(10.17 \pm 0.03)b$	$-387.35 \frac{b}{keV}$
Mo	$(177.8 \pm 0.2)b$	$(16.78 \pm 0.04)b$	$-248.94 \frac{b}{keV}$

Table 5: Computed Z-dependence factors a in $\frac{b}{keV}$ and cross sections σ in barn

Unfortunately, it was not possible to determine this relation for lead due to a lack of signal in the data leading to only having one data point for the fit. Furthermore, using only the two main emission energies asked for in the assignment, it was impossible for the fitting procedure to determine any uncertainties; this shall be discussed further below.

VI Discussion

The results from the experiment as a whole support the theory and fall in line with the general expectations for the measured spectra of the involved sources. The characteristic energy peaks are visible and their energies as measured after calibrating the channel-to-energy relation of the detector fall mostly in line with the expected values from the literature. Furthermore, the Compton continuum along with the Compton edge appear within the expected energy values from the computations, along with the peaks expected from natural sources in the background spectrum.

The analysis of the reduced Cs-137 spectrum was in line with the expectations for most of the time too. But the fact, that the literature value of the γ-energy of Cs-137 is 0.02 keV below the confidence interval of the calculated value and a reduced χ^2 parameter of the energy to channel number fit of about 6.3 suggest that the relation between energy and channel number may not be completely linear.

The calculated Compton energy of Cs-137 matches the visible Compton edge in figure 4 as mentioned above however. Even so, a slight peak is also visible to the left of the calculated Compton edge at 477.44 keV. The reason for that is the relatively slight change in deposited energy, when θ is around 180°. There is another small peak in the Compton continuum of Caesium-137 around 188 keV. This is the so called "backscatter peak". It is created by photons that got reflected at the end of the detector. Therefore those γ-rays lost an amount of energy close to the Compton energy before they got registered by the detector. The energy of the the full energy peak minus the Compton energy is marked in figure 4 as well. For the same reason that there is a small peak to the left of the Compton energy, the backscatter peak is slightly to the right of the marked "backscatter energy". The rise in count rate in the low energy part of the spectrum is likely due to electrical noise.

The estimated value of the activity of the Cs-137 source was slightly higher than expected. Compared to the value given for the experiment[1], which was approximately $2.11 \cdot 10^5$ Bq, it was about 9% higher. That error is most probably due to wrong geometrical parameters, since the detector used here, was not exactly the same as the one depicted in the data sheet. Especially the detector depth could be very different from the one indicated in the available materials.

This 9% difference, however, has no impact on the analysis of the absorbed dose during the experiment. The average absorbed dose one receives from natural background radiation during that time span (8 hours) is about $1,9 \cdot 10^{-4}$ rad in Germany[6]. Compared to that, the irradiation we received from the different samples during the experiment is about 10^3 times smaller and therefore negligible.

The analysis of the background spectrum showed that most of the background radiation in the γ-spectrum comes from the following nuclides: ^{208}Tl, ^{212}Pb, ^{214}Pb, ^{214}Bi, ^{224}Ra and ^{228}Ac. The sharp peak at the low energy end of the spectrum most likely comes from electrical noise as mentioned above as well.

Although the obtained relative detector efficiency is close to the manufacturer value for an GC2018, the validation through the rule of thumb was unfortunately not possible. This is due to the conflicting and in the case of the data sheet for the GC2018 missing detector diameter measurements. However, the 18% value is supported due to the efficiency indicated by the manufacturer being close to it at a supposed 20%. The energy resolution seems to follow an exponential dependence on the energy. Most of the data points shown in figure 8 fit the model, which gives support to the theory that the resolution follows this model for energies higher than 300 keV. The peaks at lower energies seem to behave differently though. This may be due to an at the time unknown error source, a neglected physical process or a statistical anomaly. To investigate further, more measurement would need to be taken.
As for the Peak-to-Compton ratio, more measurements with sources with few and clear defined emissions need to be taken. A linear tendency was established with the 3 data points and lies in line with the expected relationship in the literature. A clear model can not be extracted from only these three measurements however and more such data points would be needed for a compelling linear characterization of this dependence.

The measured values for the mass attenuation coefficients align well with their expected material dependence. For an increasing atomic number Z - in the case of the materials used here $Z_{al} < Z_{co} < Z_{mo}$ - the attenuation coefficient at the same energy increases as well. This proportionality between attenuation and Z can be recognized in the measured cross sections and their energy-dependence factor **a** too. These lie within the expected order of magnitude of barn as defined by $[\mu] = 10^{-28}m^2 = 1b$ and $[\mathbf{a}] = \frac{b}{keV}$. For heavier materials, the energy dependence given by **a** trends towards smaller values, as the decrease in attenuation at higher energies is smaller for materials with higher atomic numbers Z.

The main issue occurred for the measurement and computation of the relevant parameters of lead. This likely occurred because the signal was too heavily dampened by the attenuation from the lead plates. An improved measurement with thinner plates or a source with a higher activity could have provided for more sensible results here. Furthermore, using more energy peaks than just two for determining the energy dependence **a** of the cross section would have allowed for an error estimation and further discussion of the accuracy of the computed fit parameters.

In conclusion, the results support the established theory and applied simplifications within the indicated uncertainties and errors. Further measurements could lead to establishing clearer trends and decreasing these uncertainties even more, but the current ones already seem to follow the presented physical and mathematical expectations overall.

VII References

[1] Laura Rehnisch: *HLD/SCD: Gamma Spectroskopy II - Semiconductor Detector*; Vers. 1.4, 22. Oktober 2018,

[2] National Institute of Standards and Technology: *Fundamental Physical Constants*; last accessed: June 30, 2021; https://physics.nist.gov/cgi-bin/cuu/Value?esme

[3] Dr. Uwe Müller: *Physikalisches Grundpraktikum: Einführung in die Messung, Auswertung und Darstellung experimenteller Ergebnisse in der Physik*, 2007

[4] Laboratoire National Henri Becquerel:*Recommended Data* ;http://www.nucleide.org/DDEP_WG/DDEPdata.htm

[5] Tsutomu Ichimiya, Tsutomu Narita, Kensuke Kitao: *List of natural gamma-ray sources*; https://inis.iaea.org/collection/NCLCollectionStore/_Public/29/033/29033666.pdf?r=1, March 1998

[6] density of water

[7] Stadt Kölln: *Ionisierende Strahlung*; https://www.stadt-koeln.de/artikel/03065/index.html#:~:text=Also%20etwa%20Millisievert%20pro%20Jahr,k%C3%BCnstliche%20Quellen%20von%20Radioaktivit%C3%A4t%20hinzu. ; last accessed: June 30, 2021

VIII Appendix

VIII.1 Translation of sec. 7.2 Energy Resolution

The energy resolution of a coaxial detector is also measured at the 1.33 MeV spectral line of Co60 and is given as the FWHM (Full Width at Half Maximum) in keV. In practice, two lines can be separated properly, if they are at least one FWHM apart. The resolution can be determined under the same conditions as for the measurement of the efficiency mentioned above.

When measuring low activities (Low Level Measurement) it can be difficult to distinguish the signals produced by the sample from the background radiation. One can improve the results by choosing smaller energy window around the gamma peak. To do that, not only the FWHM is important, but also the peak width at a tenth of the peak hight (FWTM = Full Width at Tenth Maximum) or even a fiftieth of it (FWFW = Full Width at Fiftieth Maximum). To analyse complex spectra, the detector should show peak shapes, that satisfy the following inequalities:

$FWTM \leq 1.9 \times FWHM$

$FWFM \leq 2.65 \times FWHM$

The energy resolution of planar detectors is specified at the 122keV-line of Co^{57} by default. Meanwhile for Si(Li)-detectors, the resolution is specified to be at 5.9keV ($Fe^{5}5$).

The energy resolution ΔE^2(= FWHM in semiconductor detectors is composed mainly of three components:

$$\Delta E^2 = \Delta E_n^2 + \Delta E_q^2 + \Delta E_d^2$$

ΔE_q represents the effect of statistical fluctuations, and is calculated through the relation

$$\Delta E_q = 2.35\sqrt{F \cdot E_{pn} \cdot E}$$

(7.1)

Using the Fano-factor F, the deviation from the pure Poisson statistic is taken into account. As the generation of each -to the pulse contributing- charge carriers is not entirely independent from one another, the Fano-factor assumes a value less than one. If the value of this factor is assumed to be 0.12 and according to table 1.1 the value of E_{pn} is taken into account, the full width half maximum (FWHM) resolves to 1.62 keV at 1.33 MeV due to purely statistical effects. This value represents a limit, which can not be lowered by means of processing of the crystal or optimization of the electronics.

ΔE_n stands for the electric noise. This includes the noise of the pre-amplifier as well as the detector. To minimize the noise of the pre-amplifier, only selected field effect transistors and resistors may be used in constructing the pre-amplifier. The thermal noise of the field effect transistors is then reduced by directly connecting it with the cooled detector. The noise of the detector meanwhile, is mainly caused by leak currents and the detector capacities. The effect of the capacities is only in planar detectors of large areas noticeable. A leak current is observed when the vacuum is broken and thus the detector is not being cooled sufficiently.

Finally, the loss of charge carriers can lower the resolution, which is represented by ΔE_d. For one, during the drift (?) of a charge carrier a loss of trapping and recombination cites may occur. For another during the verification of lower energy radiation the so called "Window effect" occurs. Here, Charge carrier pairs may be created in the dead(?) layer, which then recombine before a separation is possible. Recombination losses in this dead layer and especially at trapping centres cause an asymmetric peak shape, where the peaks have long tails to the left. In this case, the detector is "taily".

When the previously described term ΔE_d is neglected, the observation that only E_q is energy dependent is made. Fig. 6.4 shows a typical behavior. Here the value of the constant electric noise was well assumed to be $\Delta E_n \approx 500eV$. At a certain "Bend energy" E_k is $[\Delta E_q = \Delta E_n]$ where in accordance to eq. (7.1)

$$E_k = \Delta \frac{\Delta E_n^2}{2.35^2.}$$

is obtained. At energies $E < E_k$ the electric noise dominates, while at energies $E > E_k$ the statistical term is higher.

VIII.2 Measurements

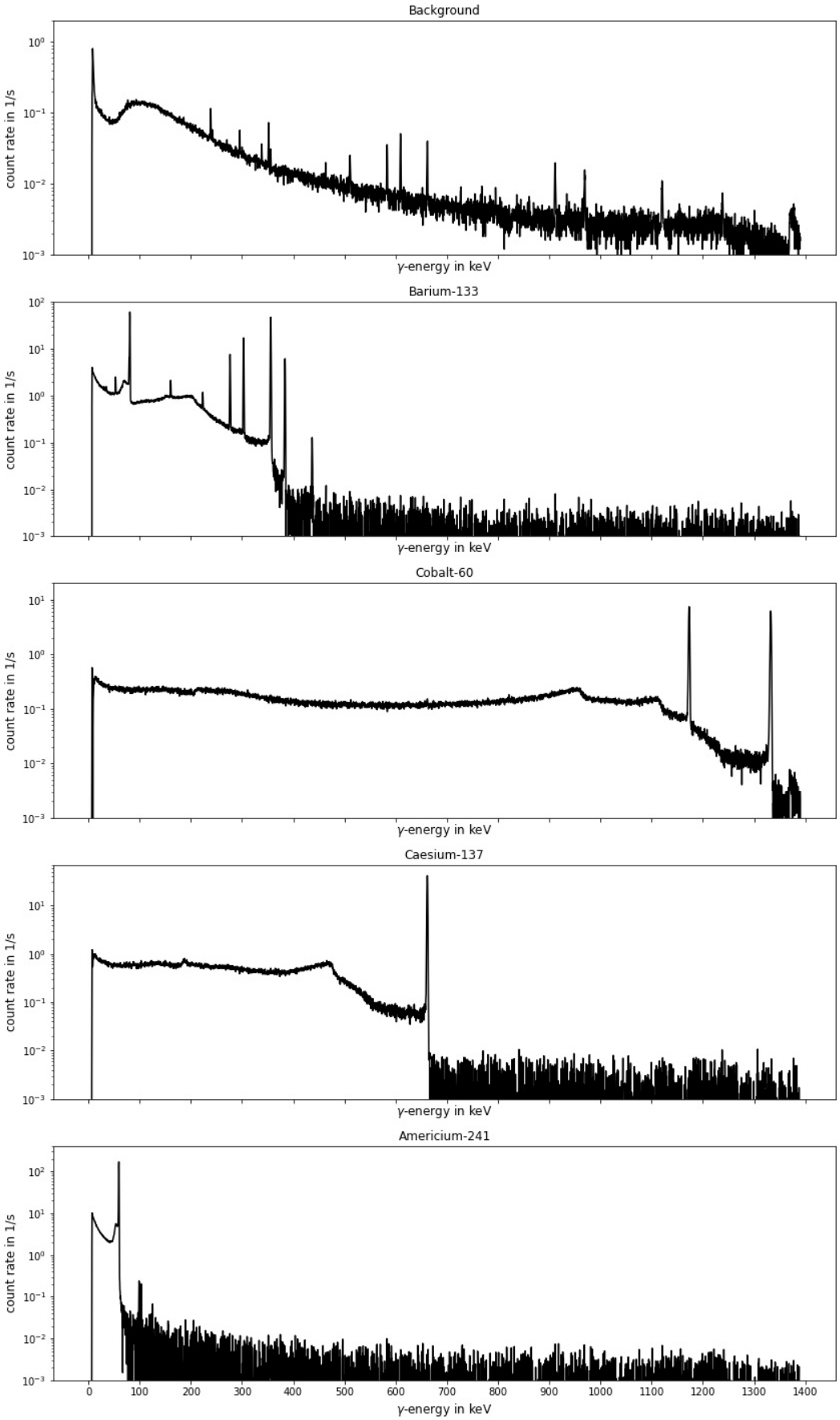

Figure 14: reduced γ-spectra of the four different sources, that were measured during the experiment, and the background spectrum